This is the peer-reviewed, final accepted version for American Mineralogist, published by the Mineralogical Society of America.
The published version is subject to change. Cite as Authors (Year) Title. American Mineralogist, in press.
DOI: https://doi.org/10.2138/am-2022-8252. http://www.minsocam.org/

Revision 2

Epidote as a conveyor of water into the Earth's deep mantle in subduction zones: Insights from coupled high pressure - temperature experiments

Lin Li[a,b,*], Chao Li[a,c], Sheng-Rong Li[a,c]

[a]*State Key Laboratory of Geological Processes and Mineral Resources, China University of Geosciences, 29 Xueyuan Road, Beijing 100083, China.*

[b]*Institute of Earth Sciences, China University of Geosciences, 29 Xueyuan Road, Beijing 100083, China.*

[c]*School of Earth Science and Resources, China University of Geosciences, 29 Xueyuan Road, Beijing 100083, China.*

*Corresponding author Email address: clark.li@cugb.edu.cn

Abstract

Epidote is a major hydrous mineral in subducted mafic oceanic crust. Understanding its stability in the subduction zone environment is important for evaluating its role as a conveyor of water into the deep earth. Here we report experimental results on epidote by simulating the high pressure-temperature (*P-T*) conditions of the plate subduction environment. We used a diamond anvil cell with an external resistance heating system, combined with in-situ X-ray diffraction (XRD) and Raman spectroscopy techniques. Experiments at ambient pressure and high temperatures indicate that epidote starts to decompose at 1223 K and breakdowns completely at 1373K. In-situ XRD analyses show no phase transition at temperatures up to 1272 K and pressure up to 14.0 GPa. Raman spectra indicate that epidote is stable at 1272 K and 14.0 GPa but the energies of two Si-O bonds (ν_2,ν_5) and one M-O bond (ν_3) increase with increasing temperature. The

cation H^+ moves for a distance when the *P-T* is increased to 13.0 GPa and 1123K. Based on the thermal structure of subducted slabs in typical hot and cold subduction zones, we infer that epidote can convey water downward into the mantle transition zone through subducted mafic oceanic crust.

Key words: Epidote; High pressure and temperature experiment; Phase stability; Structural variation; Mantle transition zone.

Introduction

Deep earth water plays an important role in the exchange of energy and materials, melting of minerals and rocks as well as concentration of ore fluids and nutrients during crust – mantle interaction. Many physical properties of minerals and rocks in the deep earth, such as the melting temperature, phase transformation, rheological behavior, electric conductivity and atomic diffusion, are closely linked with the presence of water (Karato, S. et al. 1986; Inoue 1994; Litasov, K.D. et al. 2003; Bercovici, D. and Karato, S.I 2003; Yoshino, T. et al. 2006; Nishi, M. et al. 2014). As the main component of deep earth fluids, water is also pivotal in the activation and transportation of various endogenous ore materials from their source region to the ore-forming locations (Li, S.R. et al. 2013; Guo, P. et al. 2013; Li, L. et al. 2015; Shen, J.F. et al. 2019; Li, S.R. and Santosh, M. 2014, 2017). Research on earthquake mechanism also shows that earthquake swarm, regardless of the location at the interior or margin of a plate, is related to water-dominated fluids (Kurz, J.H. et al. 2004). Water, therefore, is a key factor in the deep earth processes that controls various tectonic-magmatic-metallogenic-earthquake events.

It is now commonly recognized that water in the deep earth reservoirs can be continuously replenished through the subduction of oceanic lithosphere to the subcontinental mantle in convergent plate margins (e.g., Thompson, A.B. 1992; Poli, S. and Schmidt, M.W. 2002; Litasov, K.D. et al. 2003; Nishi, M. et al. 2014; Pamato, M.G. et al. 2015; Walter, M. et al. 2015; Liu, X. et al. 2019). Most of the information and models

so far relied mainly on seismic tomography data which suggest that oceanic lithosphere can subduct deep into the lower mantle and even accumulate at the core-mantle boundary (Maruyama, S. et al. 2007; Fukao, Y. et al. 2009; Li, L. et al. 2014 and references therein). During the subduction of ocean plate, hydrated magnesium-rich silicate minerals play a key role in carrying water to the deep earth. Earlier studies indicate that the highest-pressure hydrous magnesium-rich silicates (phase D, $MgSi_2H_2O_6$) decompose into nominally anhydrous minerals and water at about 44 GPa and at least at 1223.15K. (Shieh, S.R. et al.1998; Frost, D.J. and Fei,Y. 1998), indicating that no water can infiltrate into the lower mantle at depth greater than 1250 km. Recent experimental studies show that another hydrous silicate $MgSiH_2O_4$, named as phase H, formed from phase D, is stable at pressure of about 48 GPa (Nishi, M. et al. 2014). Since structural stability plays a decisive role as water-carrier for hydrous minerals, studies of these minerals in the oceanic plate with regard to their structural states, as well as the temperature and pressure of dehydration process, are important in gaining insights into the deep earth water reservoirs, water replenishing mechanism, the origins of mantle plume, diamondiferous kimberlite and lamproite, and various metallic deposits, as well as the mechanism of earthquakes.

Epidote is a common hydrous mineral in altered oceanic basaltic rocks and is a potentially important carrier of H_2O in subducted oceanic crust (Qin, F. et al. 2016). Previous experimental investigations on the structural stability of epidote were carried out mostly in hydrothermal systems (e.g., Fyfe, W.S. 1960; Liou, J.G. 1973; Pawley, A.R. and Holloway, J.R. 1993; Franz, G. and Liebscher, A. 2004), or under high temperature or pressure (Qin, S. et al. 2003; Liu, J. 2003; Gatta, G.D. et al. 2010, 2011; Qin, F. et al. 2016). Experiments on epidote under coupled high temperature and high pressure conditions are important to simulate the subduction zone setting. Recently, a simultaneous high pressure-temperature study of epidote found no phase transition to ~17.7 GPa and 700 K (Li, B. et al. 2021). This P-T range does not match the thermal structure of oceanic plate subduction. In this study, we report new results from a series of high-pressure and high temperature experiments on epidote. Our experiments reveal for

the first time that epidote is stable at 14.0 GPa and 1272 K, implying that epidote in subduction zone can carry water to the transition zone (between the upper mantle and the lower mantle).

Sample and experimental setup

The epidote-bearing rock specimen for this study was collected from the strongly epidotized basalt in the Qinling Triassic Orogenic Zone, Shaanxi province, China. The specimen was crushed into small pieces, and dark green epidote crystals were handpicked. After checking the purity of the grains under stereoscopic and polarizing microscopes, the chemical composition of the epidote crystals was analyzed by electron probe microanalysis. The chemical formula of the crystal sample was determined to be:

$$Ca_{1.864}Fe_{0.794}Al_{2.120}Si_{2.985}O_{12}\ (OH)$$

The crystal structure of the epidote samples under ambient conditions was analyzed by an X-ray single crystal diffractometer, Rigaku Xtalab PRO diffractometer system with HyPix-6000HE detector at the State Key Laboratory of Geological Processes and Mineral Resources, China University of Geosciences, Beijing, China. The diffraction intensity data collections were performed by a 1.2 Kw water cooled microfocus source with Mo rotor target and multilayer mirrors. Data processing was accomplished with the CrysAlisPro processing program and the crystal structures were solved by the direct methods using package SHELXS and refined in the anisotropic approach for non-hydrogen atoms using the SHELXL program (Sheldrick, G.M. 2008). The structural cell parameters of the epidote crystal (with space group $P2_1/m$) were refined at R1= 0.014 as follows:

a=8.8831(4) Å, b=5.6252(2) Å, c=10.1456(5) Å, β =115.409(5)°

High temperature powder X-ray diffraction (XRD) was performed using a Bruker D8 Advance diffractometer with Ni filtered CuKα (λ = 1.5059 Å) in Shanghai Institute of Ceramics, Chinese Academy of Sciences. The XRD pattens were obtained 30 mins after a targeted temperature point was reached. High temperature XRD data were obtained

105 from one well-ground single crystal of epidote in the steps of 50 K. Because of the small
106 amount of sample powder, the diffraction peaks from Pt heating stage shows up around
107 38° and 46°. The XRD patterns were analyzed using PDindexer software (Seto et al.
108 2010) and AMCSD (American Mineralogist Crystal Structure Database) (Downs, R.T. and
109 Hall-Wallace, M. 2003). High temperature quartz (β-quartz) (Kihara, K. 1990), anorthite
110 (Foit, F.F. et al. 1973), and magnetite (Fleet, M.E. 1984) were identified in higher-
111 temperature patterns.

112 The ambient Raman spectrum was obtained on a HORIBA LabRAM HR Evolution
113 spectrometer, equipped with 1800 lines per mm. A 532 nm wavelength laser was focused
114 on the sample; the focal spot was 2 microns wide. The CCD detector has a spectral
115 resolution less than 1cm^{-1}. The acquired spectrum was analyzed by Horiba Labspec6
116 software with the minerals database, and further analyzed by OriginPro 8.5 with a
117 Gaussian peak fitting function.

118 High pressures and high temperatures were generated by a resistance external
119 heating system set up in a Diamond anvil cell (BX90 REV Model, USA). The culet of the
120 anvils in the diamond anvil cell (DAC) had a diameter of 450μm. To avoid -OH band
121 contamination from ethanol-methanol-water mixture, we utilized silicon oil (AP 150
122 wacker, Sigma-Aldrich) as the pressure medium. Oriented single crystal epidote and fine
123 powdered sample from a single crystal were loaded in the 200μm sample chamber which
124 was drilled in a rhenium gasket for Raman spectrum analyses and synchrotron XRD
125 analyses. The K-type thermocouple was placed on the surface of the diamond anvil
126 which was surrounded by a platinum resistance heater. The temperature was measured
127 by a ST504-R11 K-type thermocouple thermometer manufactured by Shangtong
128 Instrument CO., LTD. We obtained in situ X-ray patterns and Raman spectra thirty
129 minutes after the temperature on the display of thermometer stabilized.

130 High temperature Raman scattering measurements were performed using a confocal
131 Raman system equipped with a solid state laser, while high pressure and high
132 temperature experiments were conducted with a laser wavelength of 532nm and a triple

grating monochromator (Andor Shamrock SR-303i-B, EU), combined with a CCD Model DU970P-UVB, by ANDOR Newton, EU. Before every single run, we calibrated the spectrometer by measuring a Raman spectrum of a silicon wafer (Temple, P.A. and Hathaway, C.E. 1973) with an uncertainty around 0.5cm^{-1}. Raman measurements at ambient conditions were performed by summing 10 acquisitions of 10s with an output power of 40mW. Raman spectra at high temperatures were measured by summing 20 acquisitions of 10s and 40mW.

Based on the study of Nagashima, M. (2021), and our previous work, we set the incident laser beam perpendicular to the 010 orientation of epidote in the high pressure and high temperature *in-situ* Raman spectrum measurements. By adopting this procedure, the signals from both the crystal lattice and OH- vibration in epidote can be detected appropriately. Otherwise , when incident laser beam is parallel to the 010 orientation of epidote, the OH-stretching and lattice vibrations in the high frequency part of Raman spectrum can only show very week signal noise ratio at the very beginning of high pressure and high temperature experiments in the diamond anvil cell, and even such signals will quickly disappear with increasing pressure and temperature (lattice stress and heat radiation).

In situ high-pressure high-temperature angle-dispersive XRD experiments were performed at 4W2 beamline in BSRF (Beijing Synchrotron Radiation Facility) with a monochromatic X-ray wavelength of 0.6199Å, as determined by the calibrant CeO_2, and the distance between sample and detector was 287.8mm. Pressure was measured by the ruby fluorescence spectrum (Mao, H.K. et al. 1986). The diffraction images collected by image plate detector were integrated from Debye rings and converted into one dimensional diffraction patterns using Fit2D program (Hammersley, A.P. 2016), and the X-ray diffraction patterns were fitted by PDindexer software (Seto et al. 2010).

Results

Experiments at high temperatures

Initial XRD experiments were conducted on epidote at temperatures ranging from 523 K to 1473 K in a vacuum vessel (Fig.1). These results indicated that epidote remained structurally stable until it started to decompose at 1223 K under low-vacuum environment. The complete breakdown of epidote occurred at 1373 K. The decomposition products were anorthite, quartz, and trace amount of magnetite.

Experiments at high pressures and temperatures

High pressures/temperatures experiments on epidote were carried out at pressures ranging from 0.8 GPa to 14.0 GPa and simultaneous high temperatures ranging from 297 K to 1272 K. In-situ high pressures / high temperature XRD measurements of the experiment products showed that the peaks observed in this P-T range all belong to epidote and no new peaks appeared or vanished, indicating that there were no phase transition (Fig.2).

All the Raman vibration bands of the experimental products were carefully compared with the Raman spectrum of epidote (Huang, E. 1999; Qin, F. et al. 2016) at ambient conditions in wavenumber ranges from 70 cm^{-1} to 1120 cm^{-1} (Fig.3A) and from 2500 cm^{-1} to 3800 cm^{-1} (Fig.3B). Except for some silicon oil vibrations (Figs. 3A and 3B) (Wang, X.X. et al. 2014), the rest of the Raman peaks were all generated from epidote.

At simultaneous high pressure and high temperature conditions (from 0.8 GPa to 14.0 GPa and 287K to 1272K), many weak Raman peaks of the experimental products vanish or cannot be distinguished in the Raman spectra (Fig.3C). Therefore, 7 distinguishable Raman vibration bands are selected here for further discussion. Among these, bands1, 6 and 7 (ν_1,ν_6,ν_7) were distinguished at pressures lower than 7 GPa (6.6 GPa) and temperatures lower than 580 K, whereas bands 2,3,4 and 5 (ν_2,ν_3,ν_4,ν_5) were

distinguishable at high pressure and high temperature up to 14.0 GPa and 1263 K, respectively.

By comparing with Raman spectroscopy simulation and previous Raman data at ambient conditions, the modes of seven Raman vibration bands of the experimental products are assigned (table 1). The frequencies of Raman bands 2, 3 and 5 increase with increasing pressure and temperature (Fig.3D). Raman spectra of the experimental products on epidote show two OH^- vibration peaks at around wavenumber 3400cm^{-1} with the main peak $OH(a)^-$ at about 3370 cm^{-1} and secondary peak $OH(b)^-$ at about 3420 cm^{-1}. As pressure and temperature increase, the intensity of the main peak $OH(a)^-$ is gradually weakened and broadened at the P-T condition below 10.2 GPa and 728K (Fig.4A). Because of the effect of compressive stress and thermal radiation, the change of the peak width could not be quantified. When pressure and temperature exceeded 10.2 GPa and 728K, the main peak $OH(a)^-$ became undetectable, while the secondary peak $OH(b)^-$ remained discernible until the P-T condition reached above 13.0 GPa and 1123 K.

Discussion

Low-grade metamorphism and hydrothermal activity are generally recognized as the main processes responsible for natural epidote (*sensu stricto*) formation. Epidote commonly occurs in metamorphosed basalts, gabbros and schists as well as marbles where it replaces olivine, pyroxene, plagioclase and calcite. It is also frequently found infilling vugs or veins in these rocks. The T-P conditions of these occurrences range from 523 to 673K, and from 0.1 to 0.2 GPa (Gatta, G.D. et al. 2010). Epidote of magmatic origin has also been reported in granitic rocks (Schmidt, M.W. and Poli, S. 2004; Li, L. et al. 2015). Although the stability of epidote depends on several factors, including oxygen fugacity, fluid composition, fluid pH and Al/Fe^{3+} ratio (Liou, J.G. 1973; Bird, D.K. and Helgeson, H.C. 1980; Bird, D.K. et al. 1988; Klemd, R. 2004), the pressure and temperature are the two main factors. Previous studies indicate that epidote is stable over a wide range of pressures and temperatures in continental and oceanic crust (Poli,

S. and Schmidt, M.W. 2004).

Previous high-pressure experiments revealed that the structure of epidote remained stable when pressure was increased up to 20 GPa at ambient temperature (Qin, S. et al. 2003), or at 1473 K and 9 GPa（Poli, S. and Schmidt, M.W. 2004）. Further experimental studies at ambient temperature on epidote provided no clues for phase transition by synchrotron X-ray single-crystal diffraction up to 30 GPa (10 GPa, Gatta, G.D. et al. 2011; 30 GPa, Qin, F. et al. 2016) and Raman spectroscopy up to 40 GPa (Qin, F. et al. 2016). Studies of epidote conducted at high-temperature or high pressure by in-situ single-crystal and powder X-ray diffraction at 293 K, 1070 K, 1200 K (0.0001 GPa), and 10 GPa (298 K) did not show decomposition and dehydration reaction (Gatta, G.D. et al. 2010; 2011).

Our experiments at about 0.0001GPa and high temperatures indicate that epidote begins decomposition at 1223 K and fully breaks down at 1373 K (Fig.1). Our in-situ X-ray diffraction measurements of the experimental products at high-pressures / high-temperatures show that epidote remains stable up to 1272 K at 14.0 GPa (Fig.2).

Based on Raman spectra of the experimental products at high-pressures and temperatures, most of the diagnostic peaks ($\mathbf{v_2,v_3,v_5}$) in the wavenumber range from 100 to 1000 cm^{-1} remained unchanged (Fig.3), suggesting that the epidote was stable at 1272 K and 14.0 GPa. The Raman vibration modes 2, 3 and 5 ($\mathbf{v_2,v_3,v_5}$) shifted towards higher frequencies with increasing pressure and temperature (Fig.3D), implying that the energy of the two Si-O bonds ($\mathbf{v_2,v_5}$) and one M-O bond ($\mathbf{v_3}$) increased when the temperature and pressure were simultaneously increased. Raman spectra of the experimental products of epidote in the wavenumber range from 3000 to 4000 cm^{-1} show two OH^- vibration peaks with the main peak $OH(a)^-$ located at about 3370 cm^{-1} and secondary peak $OH(b)^-$ located at about 3420 cm^{-1}. Both the secondary and main peaks weakened gradually with increasing pressure and temperature. The secondary peak $OH(b)^-$ eventually vanished when the *P-T* conditions exceeded 10.2 GPa and 723K (Fig.4A,B), and the main peak $OH(a)^-$ vanished when the *P-T* exceeded 13.0 GPa and

1123K (Fig.4C,D). This result indicates that H^+ might have moved in a certain direction and for a certain distance during *P-T* increase to 13.0 GPa and 1123K. This directed movement has also been reported in a high temperature experiment (Gatta, G.D. et al. 2012). On account of the aperiodic replacement of Al / Fe substitution and the X-ray diffraction undetectable defect, the secondary Raman peak of OH^- stretching vibrations is not predictable by theoretical analysis via space group of natural epidote. Based on the common knowledge that isomorphic substitution may cause Raman shifting, such secondary Raman peak can be inferred from existing phenomenon. If the secondary Raman peak is on the left side (lower frequency direction) of the main OH^- stretching peak, substitution should be relevant to light elements substituted by heavy elements, and vice versa (Nagashima, M. et al. 2021; Lei, L. et al. 2012; Langer, K. and Raith, M. 1974; Heuss-Aßbichler, S. and Fehr, K.T. 1997). From our results of experiments on epidote at ambient temperature in the cell chamber, the secondary Raman peak $OH(b)^-$ is located at about 3420 cm^{-1}, and the main Raman peak $OH(a)^-$ is at around 3370 cm^{-1} (Fig.3b). It is difficult to precisely detail the factors which lead to the $OH(b)^-$ vibrations in epidote, since the $OH(b)^-$ vibrations can not only be caused by isomorphic substitution in the lattice but also may be derived by activating of OH^- into Grotthuss state (Li, Q. et al. 2019). This is also described in the ice phase proton diffusion (Aoki, K. et al. 2010). In such a diffusion state, OH^- (or H^+) can easily migrate in the lattice of epidote and shows a sharp peak in the Raman spectra. From another perspective, while OH^-(or H^+) is activated, the conductivity increasement of the crystal can be easily detected (Hu, H. et al. 2016). In view of the above information, we infer that when pressure and temperature are boosted , the H^+ ion in epidote will first move along γ_1 to the anion O^{2-}, opposite to the O^{2-} in the original OH^- with a distance 0.206(5) nm, and then may move along two paths: one is along γ_2 to the O^{2-} bonded to Al^{3+} in M site with a distance 0.338(6) nm, and the other is along γ_3 to the O^{2-} bonded to another ion in M site with a distance 0.383(4) nm (Fig.5). Considering that the axis *b* is a little stiffer than the axes *a* and *c* in epidote under ambient temperature and high pressure (Qin, F. et al. 2016), and there is no other OH^- band is observed besides $OH(a)^-$ and $OH(b)^-$, the second path is more likely.

Implications

The oceanic crust was once considered insignificant in conveying water into the deep Earth because no hydrous minerals were observed to be stable over 10 GPa (e.g., Okamoto, K. and Maruyama, S. 2004; Litasov, K.D. and Ohtani, E. 2005). More recently, Fe-Ti oxyhydroxide was indicated to be stable in basalt at pressures above 10 GPa (Nishihara, Y. and Matsukage, K.N. 2016) and a continuous sequence of hydrous phases , such as lawsonite (0–8 GPa), Fe-Ti oxyhydroxide (8–17 GPa), Al-rich phase D (18–23 GPa), and Al-rich phase H (>23 GPa), were reported in subducting cold oceanic crust at temperature ≤1273 K (Liu, X. et al. 2019; Fig.6b). These results revealed the importance of oceanic crust as potential water carrier in the deep mantle.

As described above, most previous experiments on epidote were conducted at high temperature or high pressure conditions and showed no phase transition and dehydration reaction at 10, 20, 30, 40 GPa or 1200, 1473 K (Gatta, G.D. et al. 2010,2011; Qin, S. et al. 2003; Poli, S. and Schmidt, M.W. 2004; Qin, F. et al. 2016a, b). Measurements of the electronic conductivities of epidote at 0.5 – 1.5 GPa and 573 – 1273 K yielded maximum conductivity up to ~1 S/m at 1273 K, which was interpreted as the influence of dehydration of epidote at this temperature. The thermal structure of subduction slab in the typical hot (Central Cascadia) subduction zones and cold (central New Zealand) subduction zones (Syracuse, E.M. et al. 2010; Hu, H. et al. 2016; Liu, X. et al. 2019) (Fig.6a), show that both pressure and temperature will increase rapidly to about 5.5 GPa and 1073 K when the depth increases to about 160 km in cold subduction zones. Subsequently, the temperature increases slowly to about 1273 K and the pressure increases to about 14 GPa at depth of about 410 km. Therefore, experiments at constant high pressure or high temperature cannot properly simulate the environment neither in the hot, nor in the cold subduction systems.

Our coupled high *P*-*T* experiments suggest that epidote is stable without phase transition and prominent dehydration reaction at 1272 K and 14.0 GPa. Based on

seismological observations, a schematic diagram of subduction in the North Mariana trench was constructed (Fig.6) (Fukao, Y. and Obayashi, M. 2013; Kaneshima, S. 2003). In the P-T range of cold subducting oceanic crust (Fig.6a) and based on our new results, it is revealed that water can be carried into the mantle transition zone through epidote in the subducting mafic oceanic crust (Fig.6b).

Acknowledgements

We appreciate associate editors Dr. Sergio Speziale and Dr. Bin Chen and anonymous reviewers for valuable and constructive comments and suggestions which greatly helped improve the quality of this paper. We are grateful to Prof. M. Santosh and Dr. M. Alam for their kind help during the manuscript preparation and correction. This work was supported financially by the National Natural Science Foundation of China (91962101, 41603063) and Beijing Synchrotron Radiation Facility (2017-BEPC-PT-000851).

References

Aoki, K., Katoh, E., Yamawaki, H., Fujihisa, H., and Sakashita, M. (2002). Proton diffusion in high pressure ice. High Pressure Research: An International Journal, 22, 9-11.

Bercovici, D., and Karato, S. I. (2003). Whole-mantle convection and the transition-zone water filter. Nature, 425, 39-44.

Bird, D.K., and Helgeson, H.C. (1980). Chemical interaction of aqueous solutions with epidote-feldspar mineral assemblages in geologic systems; 1, Thermodynamic analysis of phase relations in the system CaO-FeO-Fe_2O_3-Al_2O_3-SiO_2-H_2O-CO_2. American Journal of Science, 280(9), 907-941.

Bird, D.K., Cho, M., Janik, C. J., Liou, J. G., and Caruso, L. J. (1988). Compositional, order/disorder, and stable isotope characteristics of aluminum/iron epidote, State 2-14 drill hole, Salton Sea Geothermal System. Journal of Geophysical Research. Part B: Solid Earth, 93(11),13135-13144.

Bird , D.K., and Spieler, A.R. (2004). Epidote in geothermal systems. Reviews in Mineralogy and Geochemistry, 56, 235-300.

Daniel, J.F., and Fei, Y. (1998). Stability of phase D at high pressure and high temperature. Journal of Geophysical Research: Solid Earth, 103, 7463-7474.

Della, V. G., Mottana, A., Parodi, G.C., and Griffin, W.L. (1996). FTIR spectroscopy in the OH-stretching region of monoclinic epidotes from Praborna (St. Marcel, Aosta valley, Italy). European Journal of Mineralogy, 8, 655–665.

Downs, R.T., and Hall-Wallace, M. (2003). The American Mineralogist crystal structure database. American Mineralogist, 88(1), 247-250.

Fleet, M.E. (1984). The structure of magnetite: two annealed natural magnetites, $Fe_{3.\ 005}O_4$ and $Fe_{2.96}Mg_{0.04}O_4$. Acta Crystallographica Section C: Crystal Structure Communications, 40(9), 1491-1493.

Foit, F.F., Peacor, D.R. (1973). The anorthite crystal structure at 410 and 830°C. American Mineralogist, 58, 665-675.

Franz, G., and Liebscher, A. (2004). Physical and Chemical Properties of the Epidote Minerals–An Introduction. Reviews in Mineralogy and Geochemistry, 56,1-82.

Frost, D,J, and Fei, Y. (1998). Stability of phase D at high pressure and high temperature. Journal of Geophysical Research: Solid Earth, 103, 7463-7474.

Fukao, Y., Obayashi, M., Nakakuki, T., and Deep Slab Project, G. (2009). Stagnant Slab: A Review. Annual Review of Earth and Planetary Sciences, 37, 19-46.

Fukao, Y., and Obayashi, M. (2013). Subducted slabs stagnant above, penetrating through, and trapped below the 660 km discontinuity. Journal of Geophysical Research: Solid Earth, 118(11), 5920-5938.

Fyfe, W.S. (1960). Stability of epidote minerals. Nature, 187,497-8.

Gatta, G.D., Meven, M., and Bromiley, G. (2010). Effects of temperature on the crystal structure of epidote: a neutron single-crystal diffraction study at 293 and 1,070 K. Physics and Chemistry of Minerals, 37, 475-485.

Gatta, G.D., Merlini, M., Lee, Y., and Poli, S. (2011). Behavior of epidote at high pressure and high temperature: a powder diffraction study up to 10 GPa and 1,200 K. Physics and Chemistry of Minerals, 38, 419-428.

Gatta, G. D., Alvaro, M., and Bromiley, G. (2012). A low temperature X-ray single-

crystal diffraction and polarised infra-red study of epidote. Physics and Chemistry of Minerals 39(1): 1-15.

Guo, P., Santosh, M., and Li, S.R. (2013). Geodynamics of gold metallogeny in the Shandong Province, NE China: an integrated geological, geophysical and geochemical perspective. Gondwana Research, 24, 1172-1202.

Hammersley, A.P. (2016). FIT2D: a multi-purpose data reduction, analysis and visualization program. Journal of Applied Crystallography, 49, 646-652.

Heuss-Aßbichler, S., and Fehr, K.T. (1997). Intercrystalline exchange of Al and Fe^{3+} between grossular-andradite and clinozoisite-epidote solid solution. Neues Jahrbuch fur Mineralogie-Abhandlungen, 172, 69–100.

Hu, H., Dai, L., Li, H., Hui, K., and Sun, W. (2016). Influence of dehydration on the electrical conductivity of epidote and implications for high-conductivity anomalies in subduction zones. Journal of Geophysical Research: Solid Earth, 122, 2751-2762.

Huang, E. (1999). Raman spectroscopic study of 15 gem minerals. Journal of the Geological Society China, 42,301–318.

Inoue, T. (1994). Effect of water on melting phase relations and melt composition in the system Mg_2SiO_4-$MgSiO_3$-H_2O up to 15 GPa. Physics of the Earth and Planetary Interiors, 85, 237-263.

Kaneshima, S. (2003). Small-scale heterogeneity at the top of the lower mantle around the Mariana slab. Earth and Planetary Science Letters, 209(1). 85-101.

Karato, S., Paterson, M. S., and FitzGerald, J. D. (1986). Rheology of synthetic olivine aggregates: Influence of grain size and water. Journal of Geophysical Research, 91, 8151-8176.

Kihara, K. (1990). An X-ray study of the temperature dependence of the quartz structure. European Journal of Mineralogy, 2(1), 63-78.

Klemd, R. (2004). Fluid inclusions in epidote minerals and fluid development in epidote-bearing rocks. Reviews in Mineralogy & Geochemistry, 56, 197-234.

Kurz, J.H., Jahr, T., and Jentzsch, G. (2004). Earthquake swarm examples and a look at the generation mechanism of the Vogtland/ Western Bohemia earthquake swarms. Physics of the Earth and Planetary Interiors, 142,75-88.

Lafuente, B., Downs, R.T., Yang, H., and Stone, N. (2015). The power of databases: the RRUFF project. In: Armbruster T, Danisi RM (eds) Highlights in

mineralogical crystallography. W. De Gruyter, Berlin, 1–30 #R040089.

Langer, K., and Raith, M. (1974). Infrared spectra of Al-Fe (III)-epidotes and zoisites, $Ca_2(Al_{1-p}Fe_{3+p})Al_2O(OH)[Si_2O_7][SiO_4]$. American Mineralogist, 59,1249–1258.Lei, L., Ohfuji, H., Irifune, T., Qin, J.Q., Zhang, X.Y., Shinmei, T., 2012. Disorder-activated Raman spectra of cubic rocksalt-type $Li_{(1-x)/2}Ga_{(1-x)/2}M_xO$(M=Mg, Zn) alloys. Journal of Applied Physics, 112, 043501.

Li, B., Xu, J.G., Zhang, D.Z., Ye, Z.L., Huang, S.J., Fan, D.W., Zhou, W.G., and Xie, H.S. (2021). Thermoelasticity and stability of natural epidote at high pressure and high temperature: Implications for water transport during cold slab subduction. Geoscience Frontiers, 12(2), 921-928.Li, L., Li, Q., Li, S.R., 2014. Low mantle perovskite: Solid solution, spin state of iron and water solubility., Acta Geologica Sinica (English Edition), 88(6), 1884-1894.

Li, L., Santosh, M., and Li, S.R. (2015). The “Jiaodong type” gold deposits: Characteristics, origin and prospecting. Ore Geology Reviews, 65, 589-611.

Li, Q., Yin, Q., Zheng, Y.S., Sui, Z.J., Zhou, X.G., Chen, D., and Zhu, Y. (2019). Insights into hydrogen transport behavior on perovskite surfaces: Transition from the Grotthuss mechanism to the “vehicle” mechanism. Langmuir, 35, 9962-9969.

Li, S.R., Santosh, M., Zhang, H.F., Shen J.F., Dong G.C., Wang J.Z., and Zhang J.Q. (2013). Inhomogeneous lithospheric thinning in the central North China Craton: zircon U – Pb and S-He-Ar isotopic record from magmatism and metallogeny in the Taihang Mountains. Gondwana Research, 23, 141-160.

Li, S.R., and Santosh, M. (2014). Metallogeny and craton destruction: records from the North China Craton. Ore Geology Reviews, 56, 376-414.

Li S.R., and Santosh M. (2017). Geodynamics of heterogeneous gold mineralization in the North China Craton and its relationship to lithospheric destruction. Gondwana Research, 50, 267-292.

Liou, J.G. (1973). Synthesis and stability relations of epidote, $Ca_2Al_2FeSi_3O_{12}(OH)$. Journal of Petrology, 14(3), 381-413.

Litasov, K.D., and Ohtani, E. (2005). Effect of water on subduction of oceanic crust into lower mantle. Geologiya i Geofizika, 45(12), 1427-1433.

Litasov, K.D., Ohtani, E., Langenhorst, F., Yurimotoc, H., Kubo, T., and Kondo, T. (2003). Water solubility in Mg-perovskites and water storage capacity in the lower mantle. Earth and Planetary Science Letters, 211,189-203.

Liu, X., MatsuKage, K.N., Nishihara, Y., SuzuKi, T., and Takahashi, E. (2019). Stability of the hydrous phases of Al-rich phase D and Al-rich phase H in deep subducted oceanic crust. American Mineralogist, 104, 64-72.

Liu, J. (2003). Structural changes of several aqueous silicate minerals at temperature and pressure. Thesis submitted to Peking University for master degree. 1-53. (In Chinese with English abstract).

Makreski, P., Jovanovski, G., Kaitner, B., Gajovic, A., and Biljan, T. (2007). Minerals from Macedonia. Vibrational Spectroscopy, 44(1), 162-170.

Mao, H.K., Xu, J., and Bell, P.M. (1986). Calibration of the ruby pressure gauge to 800 kbar under quasi-hydrostatic conditions. Journal of Geophysical Research: Solid Earth, 91, 4673-4676.

Maruyama, S., Santosh, M., and Zhao, D. (2007). Superplume, supercontinent, and post-perovskite: mantle dynamics and anti-plate tectonics on the core–mantle boundary. Gondwana Research, 11(1-2), 7-37.

Nagashima, M., Armbruster, T., Nishio-Hamane, D., and Mihailova, B. (2021). The structural state of Finnish Cr- and V-bearing clinozoisite: insights from Raman spectroscopy. Physics and Chemistry of Minerals, 48: 5. https://doi.org/10.1007/s00269-020-01129-z

Nishi, M., Irifune, T., Tsuchiya, J., Tange, Y., Nishihara, Y., Fujino, K., and Higo, Y. (2014). Stability of hydrous silicate at high pressures and water transport to the deep lower mantle. Nature Geoscience, 7. DOI: 10.1038/NGEO2074.

Nishihara, Y., and Matsukage, K.N. (2016). Iron-titanium oxyhydroxides as water carriers in the Earth's deep mantle. American Mineralogist, 101, 919–927.

Okamoto, K., and Maruyama, S. (2004). The eclogite–garnetite transformation in the MORB+H_2O system. Physics of the Earth and Planetary Interiors, 146(1), 283–296

Omma, K., and Izumi, F. (2011). VESTA3 for three-dimensional visualiza-tion of crystal, volumetric and morphology data. Journal of Applied Crystallography 44,1257–1276.

Pamato, M.G., Myhill, R., Boffa Ballaran, T., Frost, D.J., Heidelbach, F., and Miyajima,N. (2015). Lower-mantle water reservoir implied by the extreme stability of a hydrous aluminosilicate. Nature Geoscience, 8(1), 75–79

Pawley, A.R., and Holloway, J.R. (1993). Water Sources for Subduction Zone

Volcanism: New Experimental Constraints. Science, 260(5108), 664-667.

Poli, S., and Schmidt, M.W. (2002). Petrology of subducted slabs. Annual Review of the Earth and Planetary Science, 30, 207-235.

Poli, S., and Schmidt, M.W. (2004). Experimental subsolidus studies on epidote minerals. Reviews in Mineralogy & Geochemistry, 56, 171-195

Qin, S., Wu, X., Liu, J., Wu, Z.Y., Li, X.D., and Lu, A.H. (2003). Compressibility of Epidote up to 20 GPa at 298 K. Chinese Physics Letters, 20, 1172–1174.

Qin, F., Wu, X., Wang, Y., Fan, D., Qin, S., Yang, K., Townsend, J.P., and Jacobsen, S.D. (2016). High-pressure behavior of natural single-crystal epidote and clinozoisite up to 40 GPa. Physics and Chemistry of Minerals, 43, 649-659.

Seto, Y., Hamane, D., Nagai, T., and Sata, N. (2010). Development of a softwaresuite on X-ray diffraction experiments. Rev High Press Sci Technol, 20, 269–276 (In Japanese).

Sheldrick, G.M. (2008). A short history of SHELX. Acta crystallographica. Section A. Foundations of crystallography, 64(1), 112-122

Shen, J.F., Santosh, M., and Li, S.R. (2019). He-Ar, S, Pb and O isotope geochemistry of the Dabaiyang gold deposit: Implications for the relationship between gold metallogeny and destruction of the North China Craton. Ore Geology Reviews. DOI: 10.1016/j.oregeorev.2019.103229

Shieh, S.R., Mao, H.K., Hemley, R.J., and Ming, L.C. (1998). Decomposition of phase D in the lower mantle and the fate of dense hydrous silicates in subducting slabs. Earth and Planetary Science Letters, 159, 13-23.

Schmidt, M.W., and Poli, S. (2004). Magmatic Epidote. Reviews in Mineralogy and Geochemistry, 56 (1), 399-430.

Syracuse, E.M., van Keken, P.E., and Abers, G.A. (2010). The global range of subduction zone thermal models. Physics of the Earth and Planetary Interiors, 183(1), 73–90.

Temple, P.A., and Hathaway, C.E. (1973). Multiphonon Raman Spectrum of Silicon. Physical Review B, 7, 3685-3697.

Thompson, A.B., and Connolly, J.A.D. (1992). Migration of metamorphic fluid: some aspects of mass and heat transfer. Earth Science Review, 32(1-2), 107-121.

Walter, M., Thomson, A., Wang, W., Lord, O., Ross, J., McMahon, S., Baron, M., Melekhova, E., Kleppe, A., and Kohn, S. (2015). The stability of hydrous silicates in Earth's lower mantle: Experimental constraints from the systems $MgO\text{-}SiO_2\text{-}H_2O$ and $MgO\text{-}Al_2O_3\text{-}SiO_2\text{-}H_2O$. Chemical Geology, 418, 16–29.

Wang, X.X., Li, Z.H., Chen, C., Wang, K., Han, B., Zhou, Q., and Li, F.F. (2014). High Pressure Raman Spectra of Silicone Oil. Chemical Journal of Chinese Universities, 35, 2384-2389.

Yoshino, T., Matsuzaki, T., Yamashita, S., and Katsura, T. (2006). Hydrous olivine unable to account for conductivity anomaly at the top of the asthenosphere. Nature, 443, 973-976.

Captions for figures and table

Fig.1 In-situ X-ray diffraction patterns (λ=1.54 Å) of epidote with increasing temperature at atmospheric pressure. Note that the typical epidote peaks at 2Theta of 67° and 56° weakened when the temperature was increased to 1223K and these peaks fully vanished at 1373K at atmosphere pressure whereas the peaks typical for quartz, anorthite and magnetite were still present. Abbreviations: Qtz=quartz, An=anorthite, Mag=magnetite.

Fig.2 In-situ X-ray diffraction patterns (λ=0.6198 Å) of epidote at simultaneously high-temperatures and high-pressures.

Fig.3 Raman spectra of the experimental product of epidote at ambient conditions (in cell 0.6GPa and 297K) in wavenumber ranges from 70 cm^{-1} to 1120 cm^{-1} (A) and from 2500 cm^{-1} to 3840 cm^{-1} (B) (Huang, E. 1999; Qin, F. et al. 2016). In situ Raman spectra under high-pressures and high-temperatures (C) and peak shifts (D) fitting from Raman spectra. The blue diamond symbols represent the signal from silicon oil.

Fig.4 Raman spectra of experimental products of epidote. Two OH-vibration peaks (OH(a)- and OH(b)-) at P-T condition below 10.2 GPa and 723 K (A) and one (OH)-vibration peak (OH(a)-) at higher P-T condition (B) ; One (OH)-vibration peak (OH(a)-) at P-T condition below 13.0 GPa and (1123 K) (C) and no (OH)-vibration peak at higher P-T condition (D).

Fig.5 Interpretation of the possible movement paths for H^+ in epidote when the P-T conditions are increased from 10.2 GPa and 723 K to 13.0 GPa and 1123K drawn by VESTA (Momma and Izumi 2011).

Fig.6 (a) Compiled P-T range (gray area) of the cold subducting oceanic crust showing change with increasing depth. The original data are from Syracuse, E.M. et al. 2010; Hu, H. et al. 2016; Liu, X. et al. 2019. (b) Schematic diagram of subduction zone in the North Mariana trench (Fukao, Y. and Obayashi, M. 2013; Kaneshima, S. 2003) showing the stable ranges for epidote (epi), lawsonite (law), Fe-Ti oxyhydroxide (Fe-Ti), Al-rich phases D and H at the top of cool subduction zone. The blue solid circles represent the pressure and temperature conditions in this study.

Table 1 The modes of 7 lattice vibration bands and the main OH- vibration band of the experimental products of epidote at varying pressures and temperatures.

Table 1 The modes of 7 lattice vibration bands and the main OH- vibration band of the experimental products at varying pressures coupled with varying temperatures

Modes	ω_0(cm^{-1})	Assignment	Reference
ν_1	224	Ca-O	Makreski et al. 2007
ν_2	422	Si-O	
ν_3	449	M-O	Qin et al. 2016
ν_4	562	Si-O	
ν_5	597	Si-O	
ν_6	885	Si-O	Makreski et al. 2007
ν_7	913	Si-O	
ν_8	3370	-OH	Lafuente et al. 2015

Figure 1

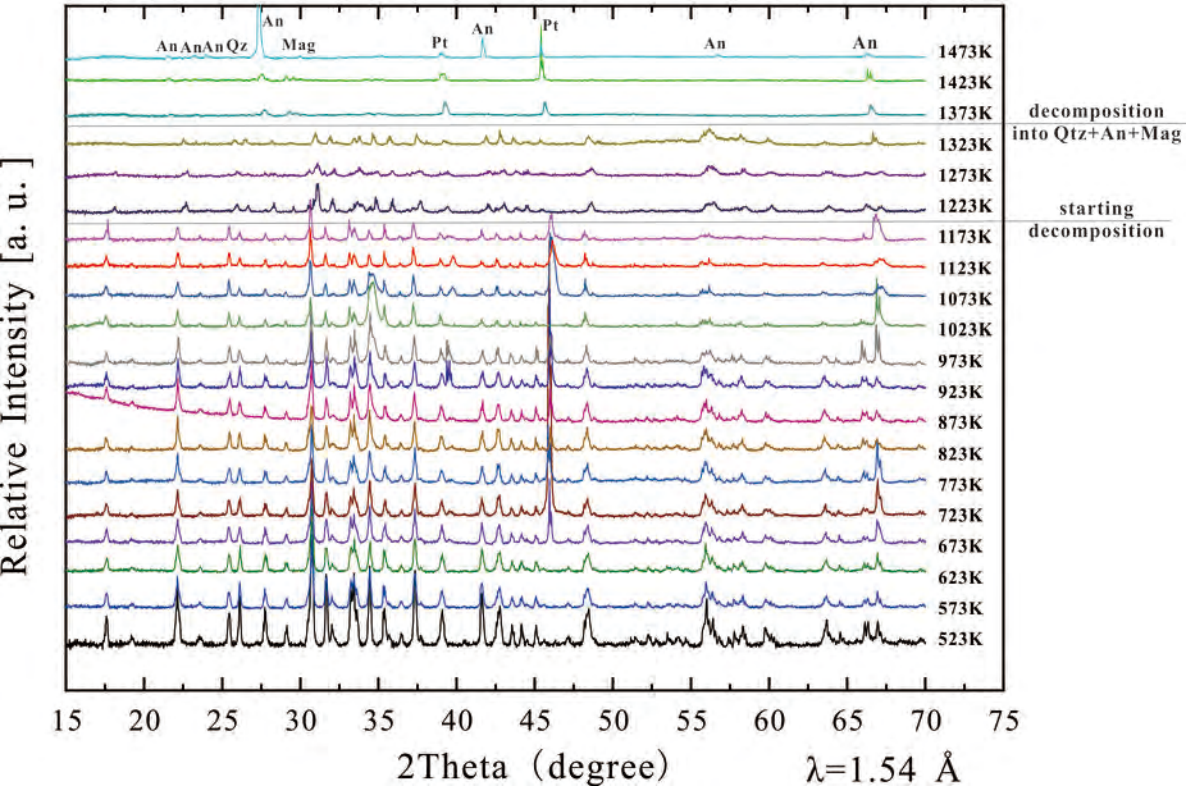
An
An An An Qz
Mag
Pt
An
Pt
An
An
1473K
1423K
1373K
decomposition
into Qtz+An+Mag
1323K
1273K
1223K
starting
decomposition
1173K
1123K
1073K
1023K
973K
923K
873K
823K
773K
723K
673K
623K
573K
523K
Relative Intensity [a. u.]
15 20 25 30 35 40 45 50 55 60 65 70 75
2Theta (degree)
λ=1.54 Å

Figure 2

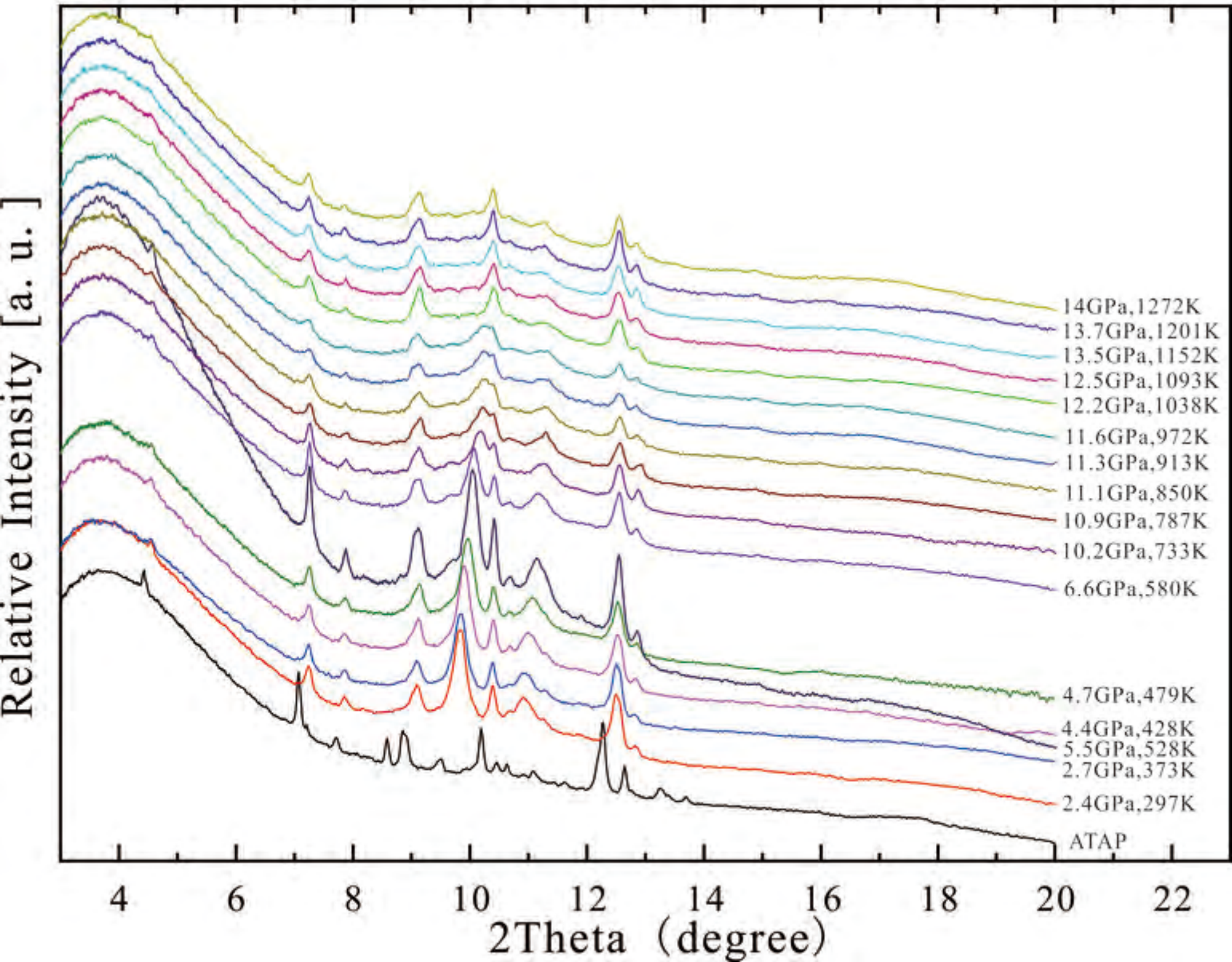
Relative Intensity [a. u.]
14GPa,1272K
13.7GPa,1201K
13.5GPa,1152K
12.5GPa,1093K
12.2GPa,1038K
11.6GPa,972K
11.3GPa,913K
11.1GPa,850K
10.9GPa,787K
10.2GPa,733K
6.6GPa,580K
4.7GPa,479K
4.4GPa,428K
5.5GPa,528K
2.7GPa,373K
2.4GPa,297K
ATAP
4
6
8
10
12
14
16
18
20
22
2Theta (degree)

Figure 3

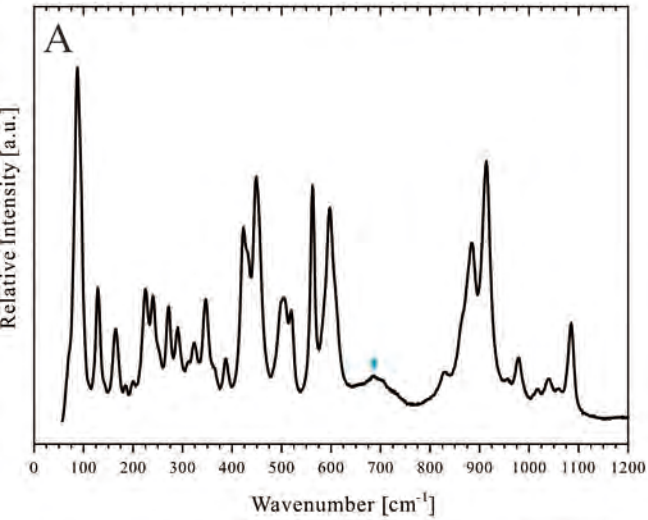
A
Relative Intensity [a.u.]
0 100 200 300 400 500 600 700 800 900 1000 1100 1200
Wavenumber [cm-1]

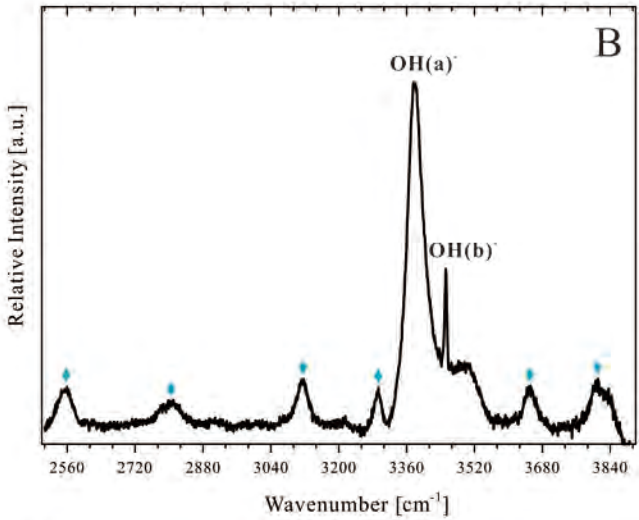
B
OH(a)-
OH(b)-
Relative Intensity [a.u.]
2560 2720 2880 3040 3200 3360 3520 3680 3840
Wavenumber [cm-1]

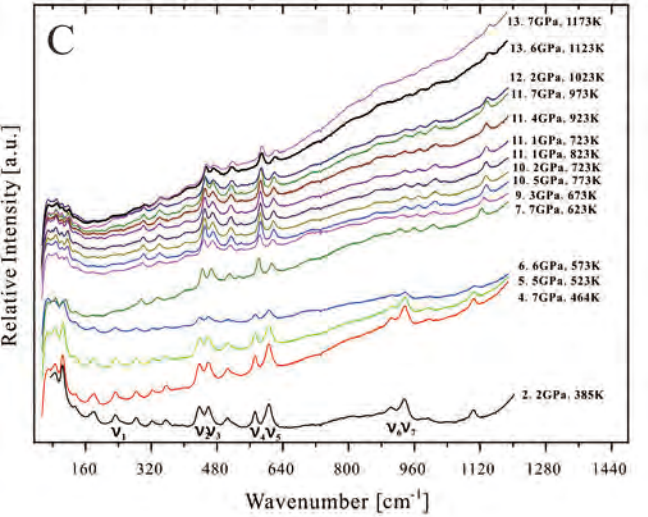
C
13. 7GPa, 1173K
13. 6GPa, 1123K
12. 2GPa, 1023K
11. 7GPa, 973K
11. 4GPa, 923K
11. 1GPa, 723K
11. 1GPa, 823K
10. 2GPa, 723K
10. 5GPa, 773K
9. 3GPa, 673K
7. 7GPa, 623K
6. 6GPa, 573K
5. 5GPa, 523K
4. 7GPa, 464K
2. 2GPa, 385K
ν1
ν3
ν4 ν2
ν6 ν7
Relative Intensity [a.u.]
160 320 480 640 800 960 1120 1280 1440
Wavenumber [cm-1]

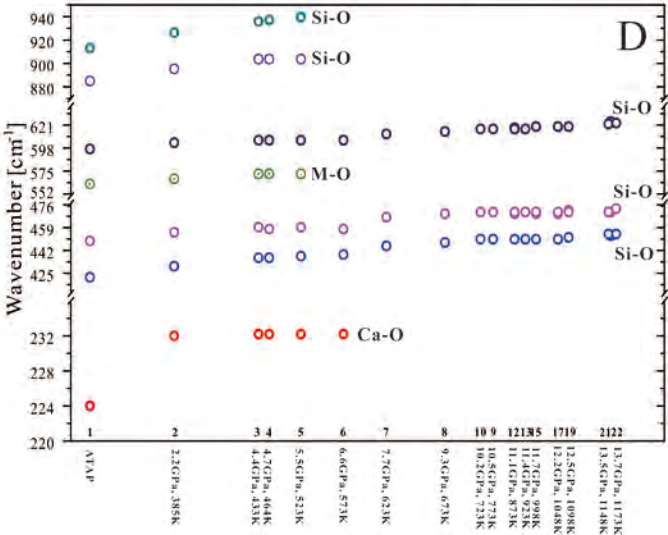
D
Si-O
Si-O
M-O
Ca-O
Si-O
Si-O
Si-O
940 920 900 880 621 598 575 552 476 459 442 425 232 228 224 220
Wavenumber [cm-1]
1 2 3 4 5 6 7 8 10 9 12 13 15 17 19 21 22
ATAP
2.2GPa, 385K
4.7GPa, 464K
4.4GPa, 433K
5.5GPa, 523K
6.6GPa, 573K
7.7GPa, 623K
9.3GPa, 673K
10.5GPa, 773K
10.2GPa, 723K
11.7GPa, 998K
11.4GPa, 923K
11.1GPa, 873K
12.5GPa, 1098K
12.2GPa, 1048K
13.7GPa, 1173K
13.5GPa, 1148K

Figure 4

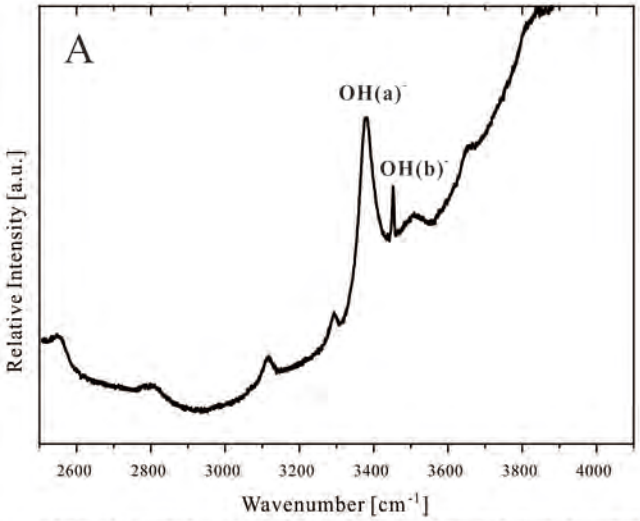
A
OH(a)
OH(b)
Relative Intensity [a.u.]
2600 2800 3000 3200 3400 3600 3800 4000
Wavenumber [cm-1]

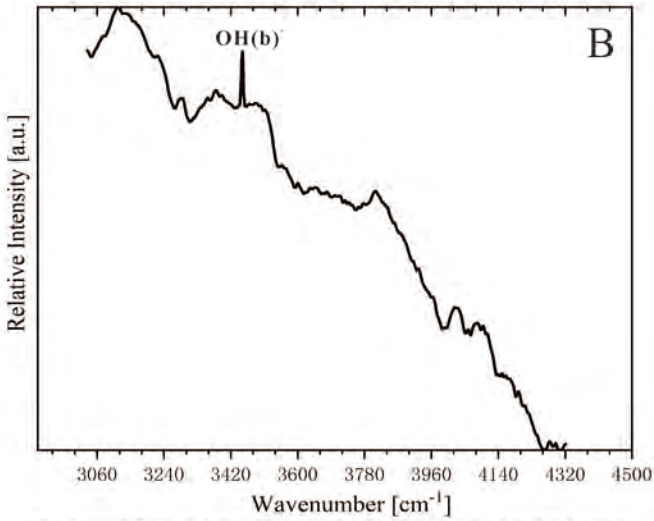
B
OH(b)
Relative Intensity [a.u.]
3060 3240 3420 3600 3780 3960 4140 4320 4500
Wavenumber [cm-1]

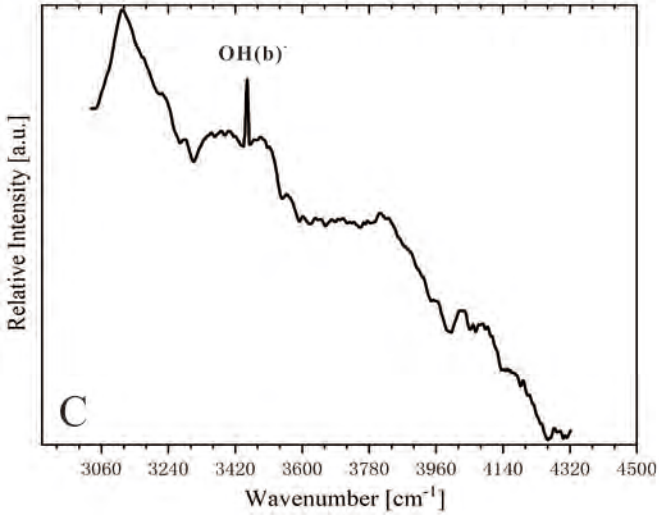
C
OH(b)
Relative Intensity [a.u.]
3060 3240 3420 3600 3780 3960 4140 4320 4500
Wavenumber [cm-1]

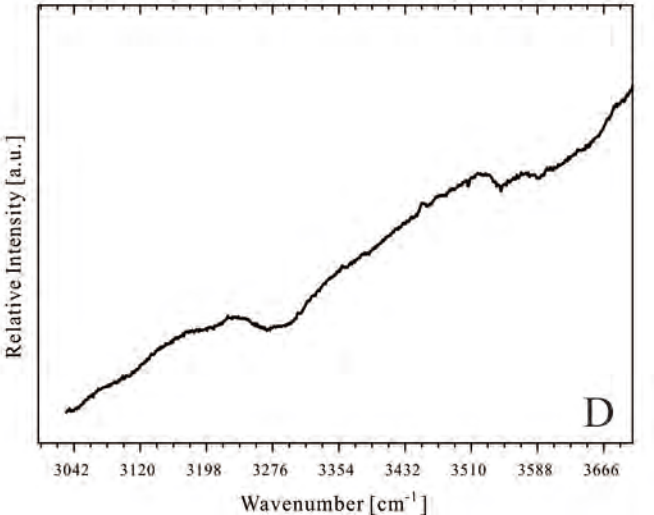
D
Relative Intensity [a.u.]
3042 3120 3198 3276 3354 3432 3510 3588 3666
Wavenumber [cm-1]

Figure 5

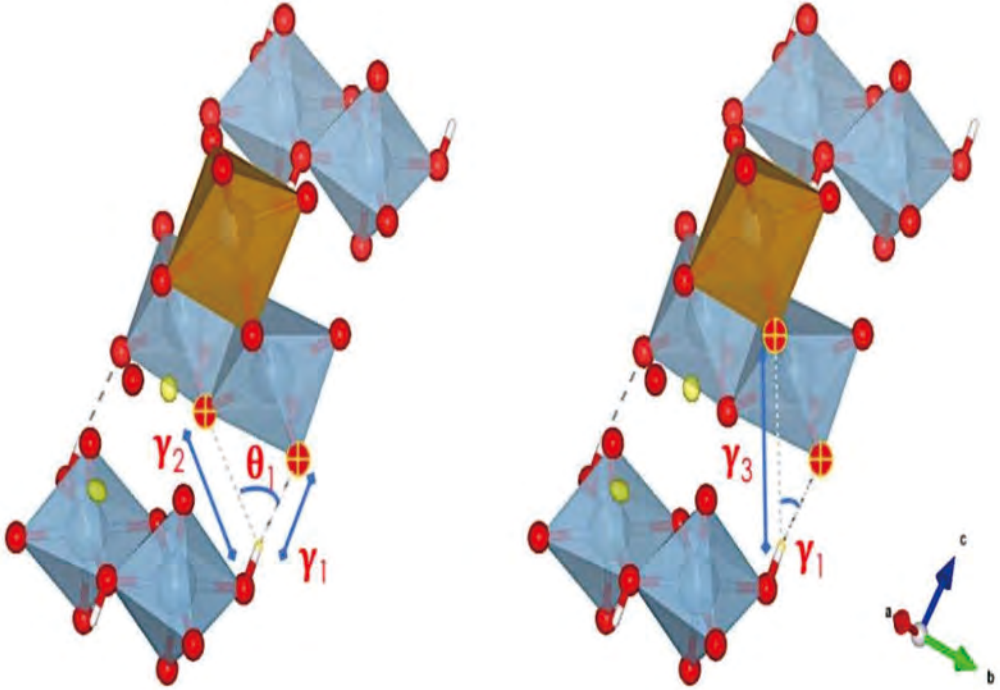

	Distance (nm)
γ_1	0.206(5)
γ_2	0.338(6)
γ_3	0.383(4)
	degree(°)
θ_1	56.4(4)
θ_2	44.4(3)

Figure 6

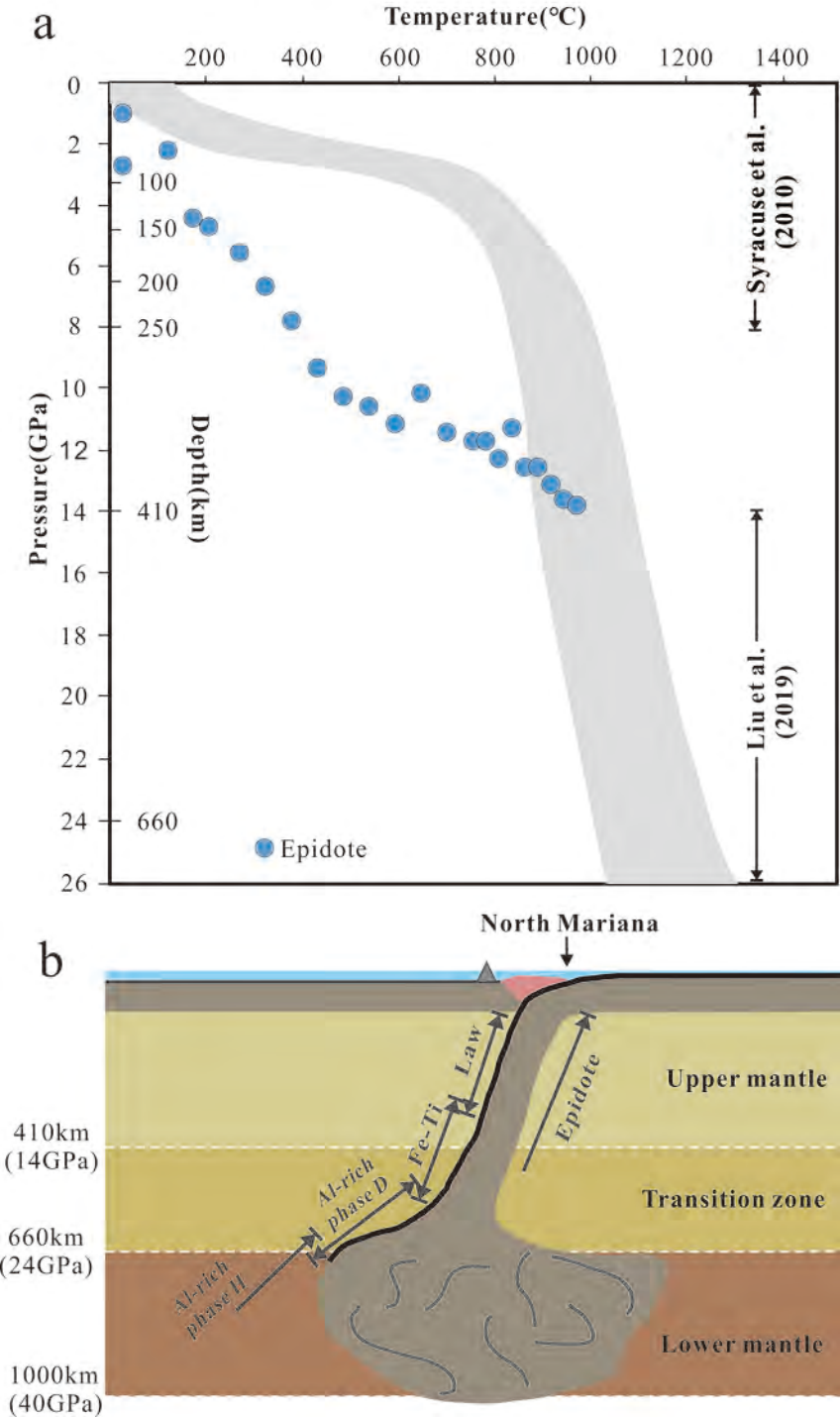
a
Temperature(°C)
200
400
600
800
1000
1200
1400
0
2
4
6
8
10
12
14
16
18
20
22
24
26
Pressure(GPa)
100
150
200
250
Depth(km)
410
660
Epidote
Syracuse et al. (2010)
Liu et al. (2019)
b
North Mariana
Law
Fe-Ti
Al-rich phase D
Al-rich phase H
Epidote
Upper mantle
Transition zone
Lower mantle
410km (14GPa)
660km (24GPa)
1000km (40GPa)